Texture evolution during nitinol martensite detwinning and phase transformation

S. Cai, J. E. Schaffer, Y. Ren, and C. Yu

Additional information on Appl. Phys. Lett.

Texture evolution during nitinol martensite detwinning and phase transformation

S. Cai,[1] J. E. Schaffer,[1] Y. Ren,[2] and C. Yu[3]

[1]*Fort Wayne Metals Research Products Corporation, 9609 Ardmore Ave., Fort Wayne, Indiana 46809, USA*
[2]*Advanced Photon Source, Argonne National Laboratory, 9700 S. Cass Ave., 433/D008, Argonne, Illinois 60439, USA*
[3]*State Key Laboratory of Heavy Oil Processing, China University of Petroleum, 102249 Beijing, China*

Nitinol has been widely used to make medical devices for years due to its unique shape memory and superelastic properties. However, the texture of the nitinol wires has been largely ignored due to inherent complexity. In this study, *in situ* synchrotron X-ray diffraction has been carried out during uniaxial tensile testing to investigate the texture evolution of the nitinol wires during martensite detwinning, variant reorientation, and phase transformation. It was found that the thermal martensitic nitinol wire comprised primarily an axial $(\bar{1}20)$, (120), and (102)-fiber texture. Detwinning initially converted the (120) and (102) fibers to the $(\bar{1}20)$ fiber and progressed to a $(\bar{1}30)$-fiber texture by rigid body rotation. At strains above 10%, the $(\bar{1}30)$-fiber was shifted to the (110) fiber by $(2\bar{1}0)$ deformation twinning. The austenitic wire exhibited an axial (334)-fiber, which transformed to the near-$(\bar{1}30)$ martensite texture after the stress-induced phase transformation. © *2013 AIP Publishing LLC*. [http://dx.doi.org/10.1063/1.4846495]

Ni-Ti alloys, especially nitinol, have been widely used in the medical industry due to their unique mechanical properties and good biocompatibility.[1,2] Simple binary Ni-Ti alloys are capable of functioning within the shape memory (thermally actuated) or superelastic (load-actuated) regimes dependent upon processing and relative operating temperatures. Such behavior is highly demanded by many minimally invasive device designers to ensure compliant, resilient, or actuated function within the targeted anatomy. For example, very high recoverable inelastic strain (e.g., superelasticity) allows a self-expanding stent to be deployed through a very small opening and spring back to bolster the arterial wall.[3,4] In fact, nitinol has dominated the medical device marketplace in high performance peripheral vascular products such as stents, guidewires, endovascular aneurysm repair devices, and embolic protection devices.[5] Proper function of such appliances depends on the orientation distribution or nanoscale alignment of atomic lattice within the population of crystals that make up the component, whether random or textured due to the crystal anisotropy.[6–8] Therefore, understanding the orientation distribution within the material and the texture evolution during transformation is important in material selection, device design, manufacturing, and application. Compared to other materials such as Ti alloys and steels, very few quantitative studies exist on texture in nitinol. A few studies exist for Ni-Ti alloys in the form of plate, sheet,[6,7,9] and recently a hot rolled bar[10,11] while very few studies have been conducted on the texture of drawn Ni-Ti wires. Gall *et al.*[12] reported a (111) austenite fiber in the cold drawn bar but did not show the texture in the stress-induced martensite. Willemse *et al.*[13] reported (110), $(1\bar{1}0)$, (101), and $(\bar{1}01)$ multiple fibers in the martensite and a (111)-fiber in the austenite of Ni-44Ti-4Cu (at. %) wire without giving details on how the texture was obtained. It appears that Willemse's paper provides the only known extant dataset informing the martensite and the austenite texture in the

Ni-Ti alloy wires. This knowledge gap is important because many of the medical devices are made of small diameter wires.[1,2] In this Letter, we report the texture evolution of a thermally martensitic wire and an austenitic wire during deformation by *in situ* synchrotron X-ray diffraction. The results provide one step towards informing nitinol wire orientation distribution and texture evolution and will be of utility to both academics and industrialists.

Two binary Ni-Ti alloys with chemical compositions of Ti-56.1 wt. % Ni (alloy 1) and Ti-55.9 wt. % Ni (alloy 5) were procured from a VAR (Vacuum Arc Melting)-melted, hot forged, hot-rolled, shaved, and cold-drawn process stream at approximately 2 mm diameter. Wire samples from these two alloys were made by a conventional multiple cold drawing and repetitive annealing process using equivalent production equipment and parameters as those used in the manufacture of nitinol wire. After the last process anneal, the sample made of alloy 1 was cold drawn to 60% reduction to a diameter of 0.3 mm; the sample made of alloy 5 was cold drawn to 40% reduction to a diameter of 0.35 mm. Both samples were then heat treated in a fluidized bed at temperature of 600 °C for 30 s followed by water quench. The grain size is about 100-200 nm. The active austenitic finish temperature (A_f) measured by DSC (Differential Scanning Calorimetry) is 244 K for alloy 1 and 374 K for alloy 5. Therefore, alloy 1 is austenitic and alloy 5 is martensitic at room temperature of about 300 K. *In situ* tensile testing was carried out at room temperature (300 K) on the beam line 11-ID-C at the Advanced Photon Source (APS) at Argonne National Laboratory. The experimental set-up was similar to that in Refs. 14 and 15, where equivalent techniques were employed to study the stress-induced martensitic phase transformation in different alloy systems such as Co alloys and beta Ti alloys. Samples were tensile deformed to a total engineering strain of 30%. X-ray diffractions were collected at selected strain levels by a Perkin–Elmer 2-D detector. The sample to detector distance
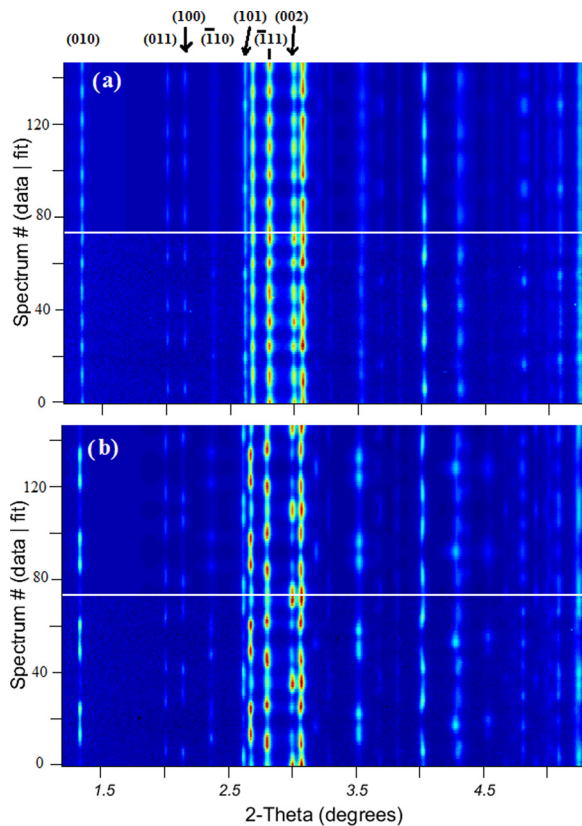
FIG. 1. Synchrotron diffraction spectra of the martensitic wire during deformation; (a) at 1.9% engineering strain, (b) at 2.1% engineering strain. The bottom of each figure shows the experimental results, the top of each figure is the result by Rietveld fit.

was ~2.2 m. The X-ray wavelength used in this study was 0.10801 Å. The beam size was ~0.2×0.2 mm^2. The instrument resolution $\Delta d/d$ was 0.2%. With this experimental setup, most of the strong diffractions, especially the first 12 peaks, were well captured as shown in Fig. 1. The "raw" data process was performed in FIT2D software,[16] and the texture was interpreted by Rietveld fitting[17] embedded in Maud[18] as described in Refs. 14 and 15. Examples are given by Figs. 1(a) and 1(b), which show diffraction spectra at the deformation strain of 1.92% and 2.12%. The lower part of each figure shows the measured diffraction spectra while the upper part of each figure shows the result of the Rietveld refinement. It can be seen that all details of the experimental result, especially the intensity patterns, were well captured by the Rietveld fitting. The change in intensity patterns between Fig. 1(a) and Fig. 1(b) is

the result of the martensite detwinning process. The fitted martensite lattice parameters before deformation are a = 2.906 Å, b = 4.659 Å, c = 4.123 Å, and $\gamma = 97.69°$.

Fig. 2 plots the inverse pole figures of the axial direction of the martensitic wire at different strain levels during deformation. It can be seen that the un-deformed material has 4 texture components. Direct pole figures suggest that they correspond to the ($\bar{1}$20), (120), ($\bar{1}$02), and (102) fiber textures. During deformation, the strength of the ($\bar{1}$20) texture component first gradually increased while the strengths of other three components gradually decreased; at the strain of ~2.1%, the (120), (102), and ($\bar{1}$02) fibers suddenly disappeared with the sharp increase in the ($\bar{1}$20) texture strength in the axial direction. Calculation of intensity centers shows that the center of the peak strength moved out from the ($\bar{1}$20) plane and formed the strong ($\bar{1}$30) fiber. The strength of the ($\bar{1}$30)-fiber first increased up to 5% strain to 15.05 multiples of random density (mrd) and began to lose strength beyond 13% (13.4 mrd) strain with intensity handed off to the (110)-fiber observed weakly at 13% strain (2 mrd) and more strongly after 30% strain. After unloading, the strength of the (110) fiber slightly decreased while the strength of the ($\bar{1}$30) fiber slightly increased.

The sharp texture change observed at ~2% strain can be explained by the martensite detwinning process. Fig. 3 shows the possible twinning systems that are responsible for the observed multiple texture components in the martensitic wire. It can be seen that the (010) compound twinning could be responsible for the observed ($\bar{1}$20) and (120) components while the [011] type II twinning likely caused the coexisting of the ($\bar{1}$20) and (102) components in the wire axial direction. Fig. 3(b) is similar to that shown in Ref. 19, but it shows that the ($\bar{1}$20) and (102) planes are almost parallel after the [011] type II twinning. The (010) compound twin is equivalent to the (001) compound twin reported in literatures that use the β angle as the non-orthogonal angle.[20] The ($\bar{1}$02) and (102) planes have the same d-spacing; thus, these two texture components can be treated as from the same group of grains. The d-spacing of the ($\bar{1}$20), (120), and (102) planes is 1.93, 1.69, and 1.67 Å, respectively. To effectively accommodate the tensile strain, detwinning likely occurred in those twinned grains oriented with the shortest d-spacing (i.e., the (120) and (102) components), giving rotation of their ($\bar{1}$20) plane-normal close to the loading direction. The reason detwinning eventually gave a strong ($\bar{1}$30)-fiber instead of a
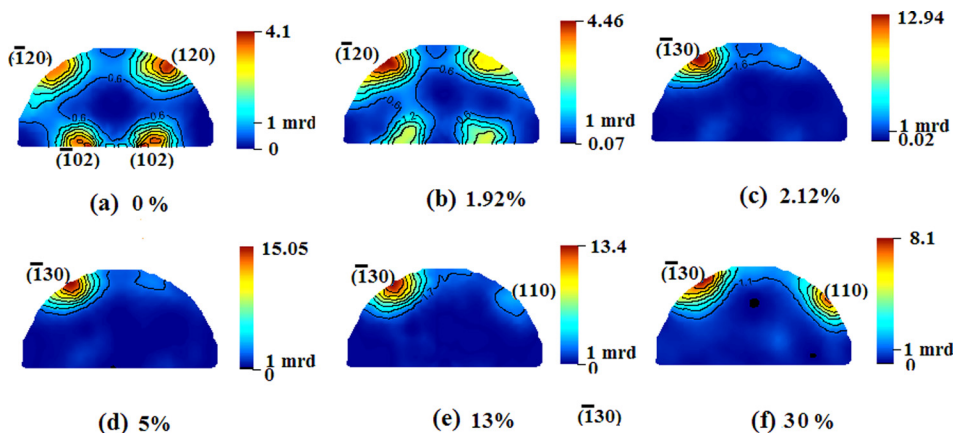

FIG. 2. Inverse pole figures of the axial direction of the martensitic wire at different strain levels. Strains are labeled at the bottom of each inverse pole figure.
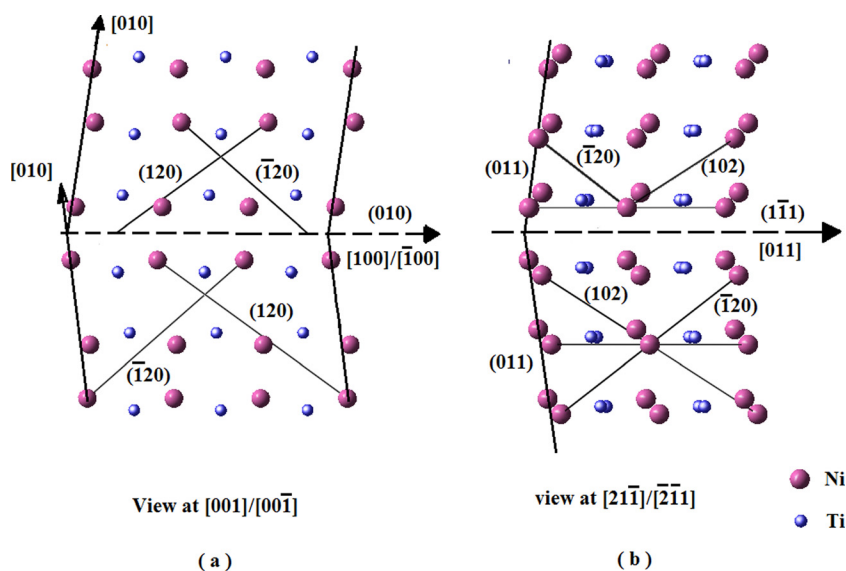
FIG. 3. (a) (010) compound twining and (b) [011] type II twinning in the martensite. Crystal structures are constructed by using the Balls & Sticks software.[22]

($\bar{1}$20)-fiber is not clear, but it may be related to the rigid body rotation associated with the martensitic transformation.[21] The texture strength increased as detwinning continued with deformation. At higher strain levels, other deformation modes were likely activated, which decreased the strength of the ($\bar{1}$30) fiber and produced the (110) texture. Previous TEM studies[23,24] showed that at strains above 7%, the martensite was deformed by the (2$\bar{1}$0)[$\bar{1}\bar{2}$0], (010)[100], and the (100)[010] compound twinning. Most recently, *in situ* neutron diffraction has been used to study the texture change of a hot rolled/drawn martensitic bar during deformation.[10,11,25] It was found that the ($\bar{1}$50) and (010) fibers formed after detwinning were shifted to the (230) texture by the (2$\bar{1}$0) deformation twinning. In the present work, considering that the angle between the ($\bar{1}$30) pole (i.e., the [$\bar{0.9}$ 1.3 0] direction) and the [120] axis is ~40°, which is very close to the angle between the (110) pole (i.e., [1.3 0.57 0] direction) and the [120] axis (~42°), an 180° rotation about the [120] twinning axis is able to bring the (110) pole to the wire axial direction, which was originally occupied by the ($\bar{1}$30) pole. However, the (010)[100] and the (100)[010] twinning systems do not have this capability. Therefore, it is very likely that the (2$\bar{1}$0) deformation twinning is also responsible for the (110) texture observed at high strains in our case. It appears that the activities of different twinning systems are more determined by the stress strain status rather than the initial textures. These data may inform why the (010) and the (100) deformation twinning systems observed in the thin film[23] and sheet[24] were not active in bar and wire samples due to the distinct sample geometries and stress strain status during deformation. More studies with different sample geometries and textures are recommended.

Fig. 4 shows diffraction spectra of the austenitic wire sample before and after the stress-induced martensite transformation. Similar to Fig. 1, the lower part of each figure shows the experimental results; the upper part shows the fitted results. It can be seen that diffraction patterns of both the austenite and martensite phases were well captured. Inverse pole figures of the austenite before deformation and the stress-induced martensite at selected strain levels are shown in Fig. 5. It can be seen that the austenite has a strong (334)

fiber texture, which is 8° away from the well adopted (111) fiber texture.[12] The reason for this difference is unknown and requires further investigation. After the stress-induced phase transformation, a strong ($\bar{2}$61) fiber texture was produced in the martensite (Fig. 5(b)). Similar to the near ($\bar{1}$30)-fiber of the martensitic wire, the strength of the ($\bar{2}$61) fiber was slightly decreased at high strains (Fig. 5(c)). The fitted lattice parameters are a = 3.016 Å for the austenite, and a = 2.900 Å, b = 4.630 Å, c = 4.150 Å, and γ = 96.49° for the stress-induced martensite phase.
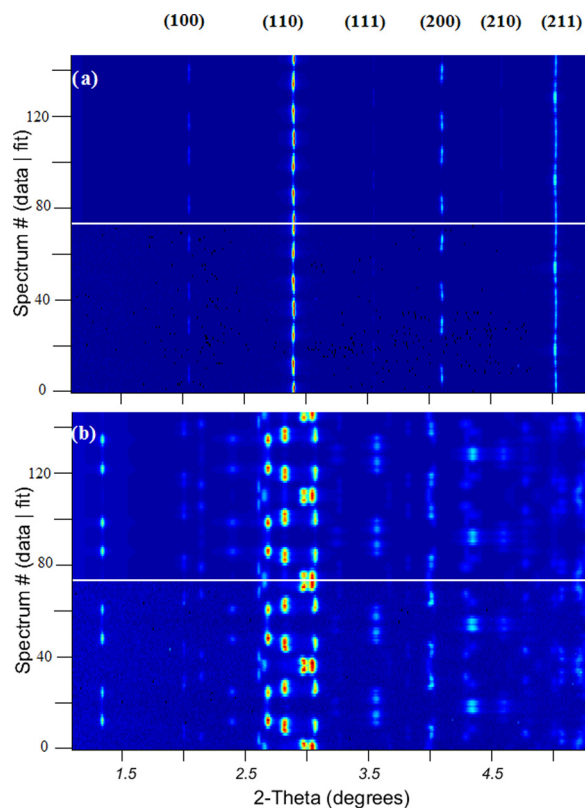

FIG. 4. Synchrotron diffraction spectra of the austenitic wire during deformation; (a) before deformation, (b) after martensite phase transformation. The bottom of each figure shows the experimental results, the top of each figure is given by Rietveld fit. Identifications of martensite peaks can be found in Fig. 1.
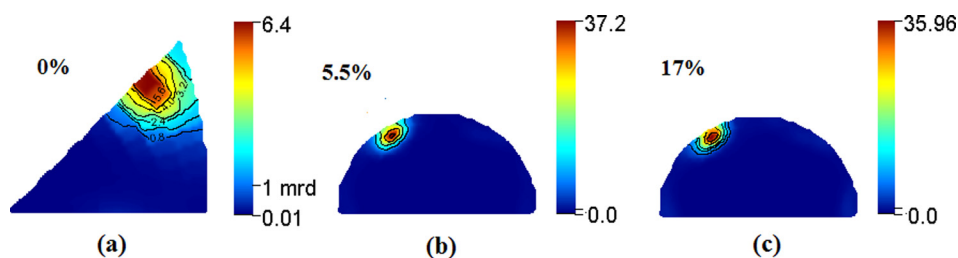
FIG. 5. Inverse pole figures of the axial direction of the austenitic wire at different strain levels; (a) austenite, (b), (c) stress-induced martensite. Strains are labeled at the upper left of each pole figure.

Based on the orientation relationship between the austenite and martensite,[26] the $(\bar{3}4\bar{3})$ austenite plane is parallel to the $(\bar{6}\bar{1}.160.17)$ martensite plane. The angle between the $(\bar{6}\bar{1}.160.17)$ plane and the $(\bar{1}30)$ plane in martensite is ~6.8° (~4.8 between the $(\bar{6}\bar{1}.160.17)$ and the $(\bar{2}61)$ planes), which is likely caused by the rigid body rotation. It is worth mentioning that, for this specific case, no precipitates or stress-induced R phase were observed during the test. Further, the volume fraction of the residual austenite was less than 3% at strains above 5.5%; thus, the influences of these factors on the texture of the SIM should be negligible. Therefore, the strong $(\bar{1}30)$ martensite fiber texture was produced from the (334) austenite texture by a lattice deformation and a rigid-body rotation. The large d-spacing of the $(\bar{1}30)$ plane makes it most favorable among all the possible variants. Fig. 5 shows that the strength of the $(\bar{1}30)$ martensite is about 6 times higher than the (334) austenite (i.e., 35.96 vs. 6.42 mrd). The change of reflection multiplicity caused by the structure change may explain this observation. The reflection multiplicity is 24 and 4 for the (334) austenite plane and the $(\bar{1}30)$ martensite plane, respectively. Thus, the random density of the $(\bar{1}30)$ martensite plane will be 6 times lower than the (334) austenite plane. The result of this is that the texture by multiples of random density of the $(\bar{1}30)$ martensite is 6 times sharper than the correspondent austenite plane.

In summary, the texture evolution of a thermal martensitic and an austenitic nitinol wire during tensile deformation were studied by *in situ* synchrotron X-ray diffraction. The thermal martensitic wire had the $(\bar{1}20)$, (120), and (102) fibers before deformation. During deformation, detwinning converted the (120) and (102) fibers to the $(\bar{1}20)$ fiber, while associated rigid body rotation led to the final $(\bar{1}30)$-fiber. At strains above 10%, the $(2\bar{1}0)$ deformation twinning caused the $(\bar{1}30)$-fiber shift towards the (110) fiber. On the other hand, the austenitic wire showed an initial (334)-fiber instead of the well-accepted (111)-fiber, which transformed to the near-$(\bar{1}30)$, $(\bar{2}61)$-fiber in the stress-induced martensite.

[1]T. W. Duerig, A. Pelton, and D. Stockel, Mater. Sci. Eng. A **273–275**, 149–160 (1999).

[2]B. Thierry, Y. Merhi, L. Bilodeau, C. Trepanier, and M. Tabrizian, Biomaterials **23**, 2997–3005 (2002).

[3]A. R. Pelton, V. Schroeder, M. R. Mitchell, X.-Y. Gong, M. Barney, and S. W. Robertson, J. Mech. Behav. Biomed. Mater. **1**, 153–164 (2008).

[4]J. E. Schaffer, E. A. Nauman, and L. A. Stanciu, Metall. Mater. Trans. B **43**, 984–994 (2012).

[5]T. W. Duerig and M. Wholey, Minimally Invasive Ther. Allied Technol. **11**, 173–178 (2002).

[6]S. Miyazaki, V. H. No, K. Kitamura, A. Khantachawana, and H. Hosoda, Int. J. Plast. **16**, 1135–1154 (2000).

[7]D. Y. Li, X. F. Wu, and T. Ko, Acta Metall. **38**, 19–24 (1990).

[8]S. Qiu, B. Clausen, S. A. Padula II, R. D. Noebe, and R. Vaidyanathan, Acta Mater. **59**, 5055–5066 (2011).

[9]B. Ye, B. S. Majumdar, and I. Dutta, Acta Mater. **57**, 2403–2417 (2009).

[10]O. Benafan, S. A. Padula II, R. D. Noebe, D. W. Brown, B. Clausen, and R. Vaidyanathan, Acta Mater. **61**, 3585–3599 (2013).

[11]A. P. Stebner, S. C. Vogel, R. D. Noebe, T. Sisneros, B. Clausen, D. W. Brown, A. Garg, and L. C. Brinson, J. Mech. Phys. Solids **61**, 2302–2330 (2013).

[12]K. Gall, T. J. Lim, D. L. McDowell, H. Sehitogluc, and Y. I. Chumlyakov, Int. J. Plast. **16**, 1189–1214 (2000).

[13]P. F. Willemse, B. J. Koopman, and J. Beyer, J. Phys. IV France **01**(C4), C4-329–C5-333 (1991).

[14]S. Cai, M. R. Daymond, Y. Ren, and J. E. Schaffer, Acta Mater. **61**, 6830–6842 (2013).

[15]S. Cai, M. R. Daymond, and Y. Ren, Mater. Sci. Eng. A **580**, 209–216 (2013).

[16]A. P. Hammersley, FIT2D V9.129 reference manual V3.1, ESRF Internal Report, 1998.

[17]H. M. Rietveld, J. Appl. Crystallogr. **2**, 65–71 (1969).

[18]L. Lutterotti, S. Matthies, H.-R. Wenk, A. S. Schulz, and J. W. Richardson, Jr., J. Appl. Phys. **81**, 594 (1997).

[19]Y. Liu and Z. L. Xie, Acta Mater. **51**, 5529–5543 (2003).

[20]M. Nishida, K. Yamauchi, I. Itai, H. Ohgi, and A. Chiba, Acta Metall. **43**, 1229–1234 (1995).

[21]Z. Nishiyama, *Martensitic Transformation* (Academic Press, New York, 1978).

[22]T. C. Ozawa and S. J. Kang, J. Appl. Cryst. **37**, 679 (2004).

[23]J. X. Zhang, M. Sato, and A. Ishida, Acta Mater. **54**, 1185–1198 (2006).

[24]M. Nishida, S. Ii, K. Kitamura, T. Furukawa, A. Chiba, T. Hara, and K. Hiraga, Scr. Mater. **39**, 1749–1754 (1998).

[25]O. Benafan, S. A. Padula II, R. D. Noebe, T. A. Sisneros, and R. Vaidyanathan, J. Appl. Phys. **112**, 093510 (2012).

[26]K. Otsuka and X. Ren, Prog. Mater. Sci. **50**, 511–678 (2005).